Synergistic Effect of Plasma and Laser Processes in Liquid for Alloyed-Nanoparticle Synthesis

Natalie Tarasenka,[1,*] Alexandre Nominé,[2,†] Alena Nevar,[1] Mikhail Nedelko,[1] Hiba Kabbara,[3] Stéphanie Bruyère,[3] Jaafar Ghanbaja,[3] Cédric Noel,[3] Andrei Krasilin,[2,4] George Zograf,[2] Valentin Milichko,[2] Nikita Kulachenkov,[2] Sergey Makarov,[2] Thierry Belmonte,[3] and Nikolai Tarasenko[1]

[1] *B.I. Stepanov Institute of Physics, National Academy of Sciences of Belarus, Minsk, Belarus*
[2] *ITMO University, Saint Petersburg, Russia*
[3] *Institut Jean Lamour, CNRS, Université de Lorraine, Nancy, France*
[4] *Ioffe Institute, Saint Petersburg, Russia*

(Received 5 March 2019; revised manuscript received 13 August 2019; published 13 January 2020)

Cu-Ag-alloy nanoparticles (NPs) are synthesized from micropowders of pure Cu and Ag by two consecutive nonequilibrium processes based on plasma and lasers in liquids. The plasma process reduces the size of the particles forming the initial powders from micrometer size to nanometer size, at which the laser fluence is sufficient to melt them, making alloying possible. Measurements at macroscopic (solution absorption), microscopic (scattering of individual NPs), and nanoscopic (electron microscopy) scales confirm alloying of NPs and homogenization of size and composition. This has a noticeable effect on the final colloidal solution, which absorbs yellow-orange light (550–600 nm) after laser treatment. With a synthesis rate of 360 mg/h, this process opens up possibilities for nonequilibrium nanometallurgy of functional NPs.

DOI: 10.1103/PhysRevApplied.13.014021

I. INTRODUCTION

Production of nanoparticles (NPs) is a large market with applications in various fields, such as catalysis [1], solar energy [2], energy storage [3,4] bioimaging [5,6], drug delivery [7,8], and light manipulation [9]. These fields are directly connected to societal challenges such as global warming, sustainable use of resources, or treatment of cancer. Therefore, the level of device performance associated with these challenges necessitates going beyond the conventional approaches and conventional materials [10,11].

One direction consists in tailoring NPs by their shape [12,13], another direction consists in tuning their composition [14], and the combination of both is also actively investigated [15–17]. In addition to these features, the question arises of the process that would ideally combine the following merits: being upscalable, fast, environmentally friendly, efficient, and inexpensive.

Nonequilibrium processes (e.g., laser-induced [18], plasma-enhanced [19], microwave-assisted [20], and carbothermal [14] processes) are attracting increasing attention for the synthesis of complex nanomaterials (alloys, core-shell nanomaterials, multimetallic nanomaterials) as they involve both locally and temporally extreme conditions of temperature and pressure (and their gradients) that could not be attained otherwise [21]. If very locally the temperature reaches several thousand degrees and pressure reaches several hundred bars, all these processes are macroscopically performed at room temperature and atmospheric pressure, which is a strong asset for industrial development.

Among the nonequilibrium processes, electrical discharges submerged in liquids are ultrafast processes to synthesize NPs from bulky electrodes [22–24]. They have the main advantages of being inexpensive, safe and easy to use. They have been successfully used to synthesize core-shell NPs [25,26] and nanosheets [25], and even to discover new crystallographic phases [27]. However, these processes do not provide sufficiently narrow size distributions yet.

Laser synthesis and processing for nanomaterial synthesis has been extensively studied in the past decade [28–32]. The most widespread process is probably laser ablation in liquids, which is usually applied to bulk targets [33–36]. Another approach, known as laser melting in liquids [37,38], consists in irradiating a colloidal solution with a laser beam. This leads to local melting of NPs with the possibility of adjusting their size at the submicrometer or nanometer scale [39]. Laser melting in liquids has also been successfully used to alloy NPs by mixing

*natalie.tarasenka@dragon.bas-net.by
†alexandre.nomine@metalab.ifmo.ru

two colloidal solutions of pure compounds and subsequent irradiation of the mixture by a nanosecond-pulsed laser [40,41].

In the present study, we investigate the combination of a plasma process, which is efficient in reducing the mean size distribution of microscopic particles to the nanoscale, and laser post-treatment of the plasma-treated colloidal solution, which is expected to promote alloying of particles. We use the Cu-Ag system as a model system. Firstly, the phase diagram is simple, with low solubility limits, the absence of a defined compound, and a single eutectic [42]. Secondly, this system is considered as a potential low-cost alternative to Au and Pt in catalysis [43] or photonics [44]. Thirdly, the Cu-Ag system could be used in a large range of applications in medicine [44], sensing [45], and microelectronics [46], and has even been found in archaeological remains [47,48].

The present study focuses on bridging the synthesis process, NP characterization, and optical properties.

II. MATERIALS AND METHODS

A. Synthesis

NPs are prepared by a two-step process consisting of electrical discharge treatment of a mixture of Ag and Cu micropowders dispersed in ethanol followed by laser irradiation of the colloid formed. First, a 1:1 mixture of Ag and Cu micropowders is dispersed in ethanol and processed in the suspension by submerged electrical discharges. For the synthesis of alloyed NPs from a mixture of precursors (powders with particles of micrometer size), a reactor cell with a special discharge configuration is constructed.

The discharge is ignited in the fluoroplastic funnel-shaped cell between two coaxial vertically orientated tungsten electrodes [Fig. 1(a)]. The conical shape of the cell prevented removal of particles from the discharge area, providing plasma processing of particles during a suitable time interval. The optimal distance between the electrodes is kept constant at approximately 2 mm to maintain a stable discharge. The discharge is initiated by application of a high-frequency voltage of 8.5 kV. The power supply provides an alternating current that feeds a spark discharge at a repetition rate of 100 Hz. The electric circuit with a relaxation time pulse generator provides a typical oscillating discharge current with high peak intensity (10–12 A) and a duration of a single discharge pulse of 2–5 μs. Oscillations are damped quickly with a decay time of 40–50 μs. The overall duration of the plasma-treatment process is 5 min.

After the discharge treatment, the colloids prepared are exposed to laser radiation. The colloidal solution obtained after plasma treatment is first diluted in ethanol in a 1:1 ratio. This solution is then exposed for 5 min to a Nd:YAG laser beam (LOTIS, wavelength 532 nm, pulse-repetition frequency 10 Hz). The pulse energy is 60 mJ over a pulse duration of 10 ns. The beam diameter is estimated as 5 mm, the fluence is 0.3 J/cm^2, and the irradiance $\Phi = 3 \times 10^{11}$ W/m^2.

Because of residual microparticles that have been filtered before further analysis, it remains difficult to accurately determine the NP production rate. However, we estimate this to be around 360 mg/h. The estimation of the concentration of the elements in the colloid prepared is performed by inductively-coupled-plasma optical emission spectroscopy calibrated by standard water solutions.

B. Plasma diagnostics

Spectroscopic studies of plasmas are performed with a diffraction spectrometer equipped with a CCD linear array. Plasma-discharge spectra are recorded with an S3801 spectrograph (Solar TII) with a focal distance of 380 mm and an input aperture of 1:4.7 that is equipped with a grating with 600 grooves/mm (inverse linear dispersion 4 nm/mm). The light emitted by the plasma is focused by lenses with a focal length of 15 cm on the entrance slit of the spectrometer to investigate the spectral region from 300 to 700 nm. The spectrograph photodetector includes a Toshiba 1205D CCD linear image sensor with 2048 LEDs (14×200 μm^2). The detection window is set to approximately 500 μs, accumulating about 100 oscillating discharge-current pulses (see Sec. II A). Thus, the registered spectra are the spectra averaged over the indicated time interval. The operation of the detection system is controlled by a computer via a USB interface with use of the CCD software tool. The identification procedure takes

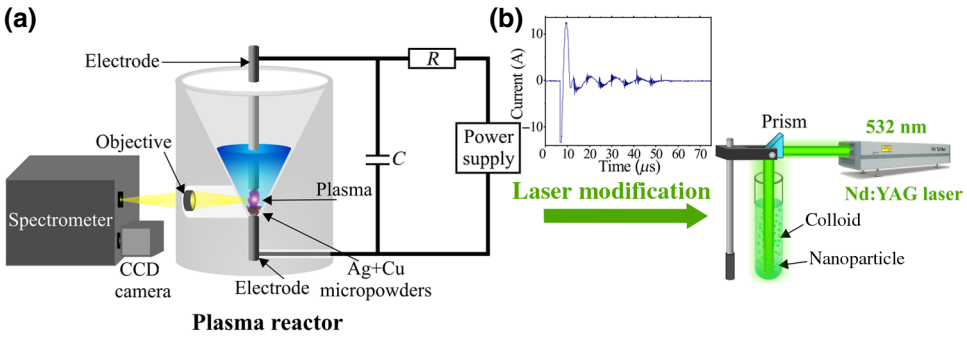

FIG. 1. The two-step process with plasma treatment (a) followed by laser treatment (b). C, capacitor; R, resistor.

into account the spectral positions of the lines and their intensities (height of the line minus the background) in comparison with the relative intensities (or transition probabilities) provided by the National Institute of Standards and Technology, NIST Atomic Spectra Database.

C. Characterization

TEM investigations are performed with a JEM-ARM200F cold-field-emission-gun transmission electron microscope and scanning transmission electron microscope operated at 200 kV and equipped with a spherical aberration (Cs) probe and image correctors (point resolution 0.12 nm in TEM mode and 0.078 nm in STEM mode).

UV-vis absorption spectra of colloidal solutions are recorded immediately after preparation in a 0.5-cm quartz cuvette with a Cary 500 spectrometer. Plasmon resonance of individual NPs is determined by white-light scattering in the dark-field geometry. For this, a droplet of solution is deposited onto a fused-silica substrate. The subsequent solvent evaporation leaves NPs on the substate with a low surface density (typically 0.1 particle/μm^2). A homemade dark-field scheme is used [49], where the NPs are illuminated by *s*-polarized light from a halogen lamp (HL-2000-FHSA) at an angle of 65° with respect to the substrate normal. The scattered signal is collected by an objective (Mitutoyo M Plan APO NIR 50, NA of 0.45) and then analyzed by a commercial confocal spectrometer (Horiba LabRam HR with a cooled CCD camera, Andor DU 420A-OE 325, and diffraction grating with 600 grooves/mm).

III. RESULTS

A. Optical properties of NPs

The effect of combined plasma and laser treatment is visible to the naked eye [Fig. 2(a)]. Firstly, the residue settled at the bottom of the vessel after plasma treatment disappears during laser treatment. Secondly, the colloidal solution changes from being slightly turbid and colorless to a well-defined orange. This is associated with a decrease in absorption over the whole visible spectrum [Fig. 2(b)] and also with the appearance of an absorption hump at yellow-orange wavelengths (550–600 nm).

Observation of NPs in the dark-field configuration [Fig. 2(c)] reveals the presence of a large amount of nanoscatterers, equally before and after the laser treatment. However, after plasma treatment only, light scattering—attributed to localized surface plasmon resonance (LSPR)—is observed within the range from 670 to 730 nm, while after the laser treatment, LSPR is blueshifted to the range from 550 to 640 nm [Fig. 2(d)]. A narrowing of the LSPR profile is also associated with laser post-treatment.

B. Characterization of NPs

Figure 3 shows that the plasma treatment significantly reduces the average size of pristine particles. Indeed, from an initial average diameter of 1 μm, particles are reduced in size to the nanometer range. In Figs. 3(d) and 4, one can notice that the size reduction is more efficient for Ag-rich particles, which have a radius range of 10–60 nm, than for Cu particles, which have a radius range of 15–275 nm. This effect is erased by the subsequent laser post-treatment that

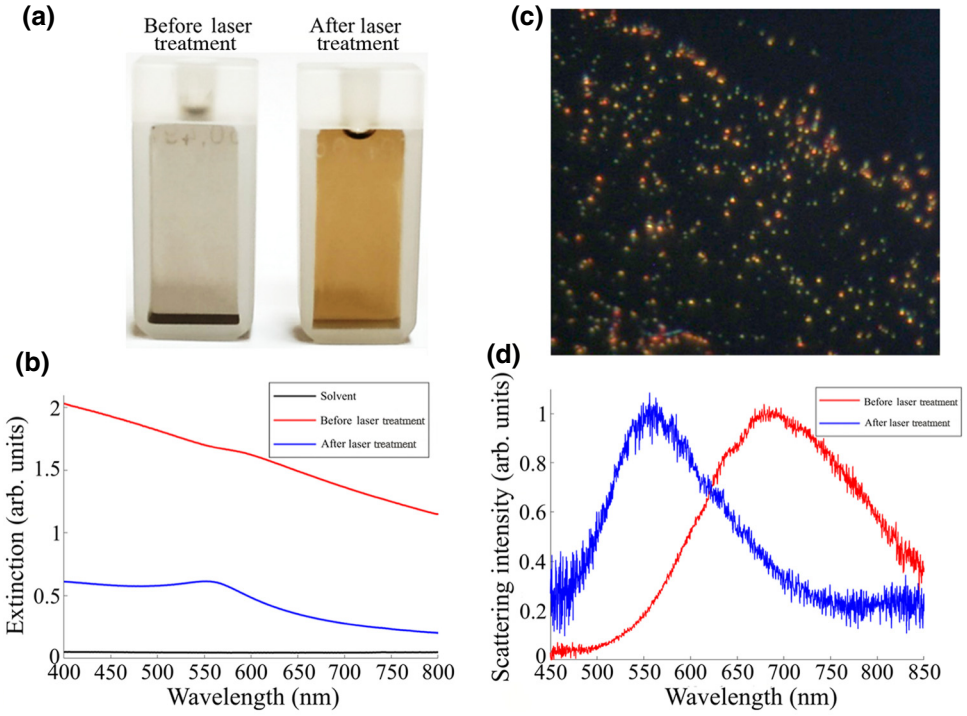

FIG. 2. (a) Images of colloidal solutions before and after laser treatment and (b) associated extinction spectra. (c) Micrograph in the dark-field configuration of the sample after laser irradiation revealing the presence of nanoscatterers and (d) their associated scattering spectra.

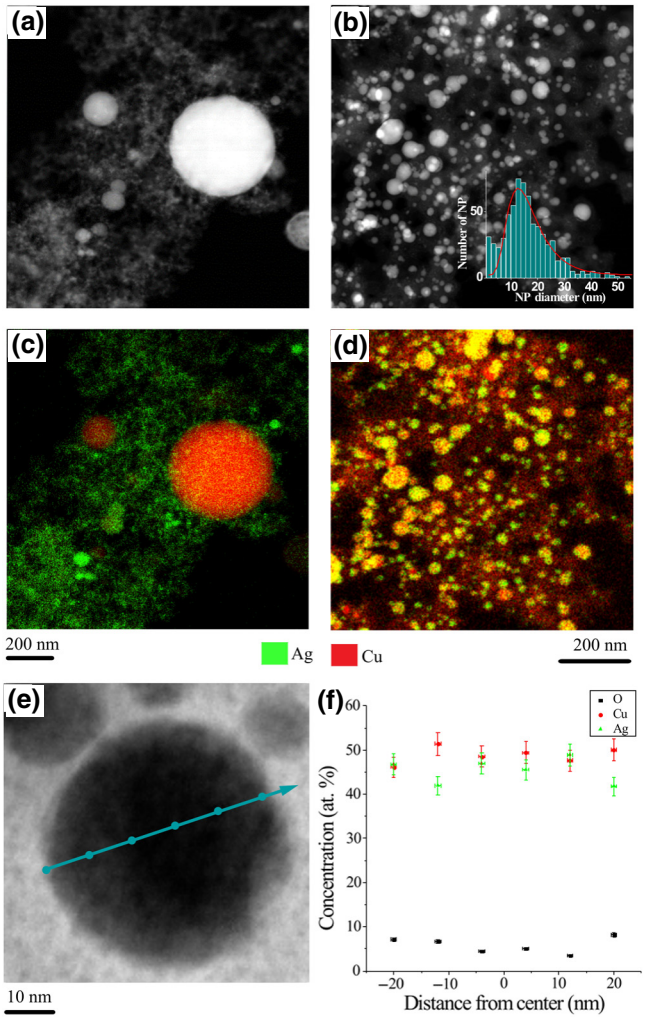

FIG. 3. (a),(b) STEM high-angle annular-dark-field micrographs and (c),(d) EDS mapping of Cu-Ag NPs synthesized by (a),(c) plasma treatment and (b),(d) combined plasma and laser treatment. (e) Line profile of EDS measurements and (f) the evolution of the concentration of Cu, Ag, and O within a single NP.

homogenizes the NPs, regardless of their composition, to a radius range of 10–65 nm (Fig. 4).

Alloyed NPs are observed after the sole plasma treatment, unlike what was reported for a pin-to-pin configuration, with electrodes made of pure Cu and Ag [50]. This shows some difference in the physical processes involved when powders are used rather than a bulk electrode as the initial source material. However and, as suggested above, the composition distribution is particularly broad (Fig. 4). A significant proportion of NPs remains unalloyed and coexist with alloyed NPs, covering the full composition range. After the laser treatment, the composition distribution is narrowed toward the composition range of 37–70 at. % Cu.

Element mapping by energy-dispersive x-ray spectroscopy (EDS) (Fig. 3) reveals a small admixture of

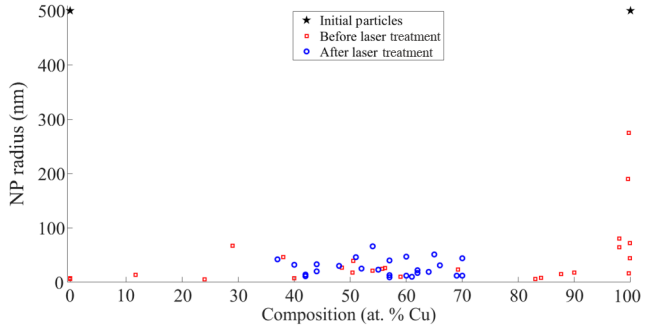

FIG. 4. Size and composition distrbution of initial microparticles, nanoparticles after plasma treatment, and nanoparticles after laser treatment.

oxygen. According to Fig. 3(f), oxygen is a minor impurity in comparison with Ag and Cu. This is related to the mechanisms of ethanol decomposition under discharge conditions. As stated in a number of publications, oxidation is not an effective process during electrical discharge and laser ablation in ethanol [51–53]. This is because thermal decomposition of ethanol occurs by dissociation of C—C or C—O bonds, resulting in by-products such as C_2H_4, CH_4, CH_3COH, etc. and radicals (including CH_3), which then react with ethanol molecules and their decomposition by-products, participating in chain reactions with dominant formation of carbide phases. So the conditions during the electrical discharge in ethanol are more favorable for the formation of carbides than oxides. However, carbide phases are also not observed since copper does not react with carbon even at high temperatures.

C. Plasma diagnostics

Typical optical emission spectra of the plasma formed during electrical discharge processing of a mixture of Ag and Cu powders are presented in Fig. 5(a). These spectra reveal the presence of spectral lines of Cu and Ag atoms (Cu I 510.55 nm, Cu I 521.77 nm, Ag I 520.82 nm, Ag I 546.30 nm) as well as Cu and Ag ions (Cu II 505.30 nm, Ag II 539.98 nm) along with Hα and Hβ lines [Figs. 5(a) and 5(b)] and the C_2 Swan band [Figs. 5(a) and 5(c)]. The presence of metallic excitation lines comes from micropowders and nanopowders, while the hydrogen lines and the C_2 band are related to ethanol decomposition. The analysis of the Hα-line broadening [Fig. 5(b)] allows the determination of the plasma electron density n_e with use of the relation for Stark broadening [54]:

$$\Delta\lambda = 2.5 \times 10^9 \times \alpha_{H\alpha} \times n_e^{2/3}, \quad (1)$$

where $\alpha_{H\alpha}$ is the broadening parameter and $\Delta\lambda$ is the full width at half maximum of the Hα line calculated from a Lorentzian fit. The measured broadening $\Delta\lambda$ is 1.86 nm and the calculated electron density is 3.3×10^{17} cm^{-3}.

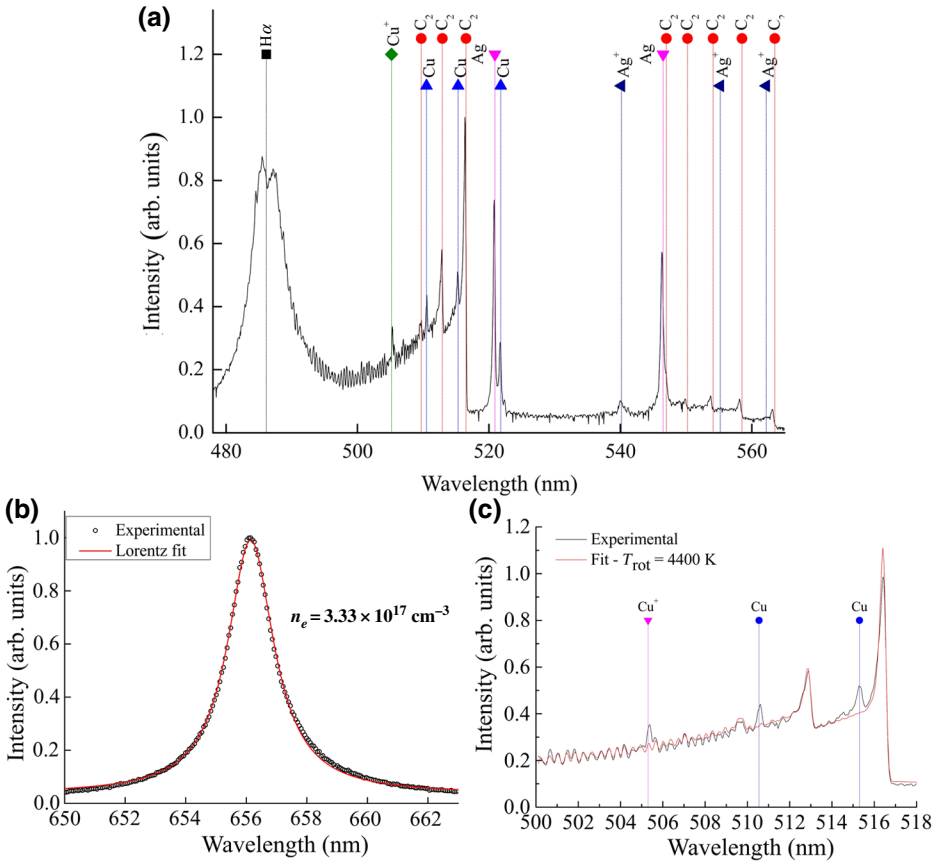

FIG. 5. Optical emission spectra showing the presence of both metallic elements as well as C_2 and H lines (a), the Hα-line profile used to determine the electron density (b), and the molecular C_2 Swan system used to determine the rotational temperature (c).

IV. DISCUSSION

A. Formation of NPs

1. Plasma process

Determination of the plasma temperature, especially with the aim of specifying the conditions of synthesis of materials, necessitates several precautions [55,56]. A common pitfall is to consider the electron temperature T_e equal to the gas temperature T_{gas} and integrate it directly in further thermal-transfer calculations. Actually, the transition levels of excitation processes are in the range of several elecronvolts (i.e., several tens of thousands of kelvins), those of vibrational levels are in the range of a few tenths of an elecronvolt (i.e., several thousand kelvins), and those of rotational levels are in the range of a few hundredths of an elecronvolt (i.e., several hundred kelvins). Therefore, the following ranking can be established:

$$T_{ex} \approx T_e \geq T_{vib} \geq T_{rot} \approx T_{gas}. \quad (2)$$

The only case when T_e may be directly considered as the process temperature is when the discharge is at thermodynamic equilibrium. Since this is the exception rather than the rule in low-temperature plasmas, it is always preferable to use the rotational temperature to estimate the gas temperature when possible. Here, the gas temperature is determined by the rotational temperature of the C_2 Swan band [Fig. 5(c)]. For a diatomic molecule, the emission intensity is given by Eq. (3):

$$I(\lambda) \propto S\left(n', v', J', n'', v'', J''\right) \exp\left(-\frac{E_{n'',v'',J''}}{kT_{rot}}\right), \quad (3)$$

where S is the oscillator strength of the transition, E is the energy of the upper level, and n, v, and J refer, respectively, to electronic, vibrational, and rotational excitation levels from upper and lower states of the transition. A least-squares method is used to get the best agreement between the experimental spectrum and the calculated spectrum with T_{rot} as an optimization variable.

In the present case, the best fitting result is found for a rotational temperature of 4400 $\pm$ 100 K. It should, however, be noted that this value is averaged over the whole discharge and postdischarge, which includes a rapid heating and cooling. Therefore, the value of 4400 K is a lower limit of the plasma temperature, which is already several times above the melting temperatures and even the vaporization points of silver and copper [57]. Despite these presumably favorable conditions, the alloying efficiency of the plasma process is low, as discussed previously [Fig. 3(c)]. This can be attributed to two main reasons:

(a) The small discharge volume, about 10^{-5} mm^3 only. The discharge volume that is at high temperature is only a small fraction of the total reactor volume.

(b) The high pressure reached during breakdown generates an "explosionlike" force field that pushes NPs far from each other [58].

If these conditions are not optimal for alloying, they are perfectly suited to reducing the size of microparticles.

2. Laser post-treatment

The models of laser interaction with colloidal nanoparticles are based on the balance between the laser energy absorbed by the NPs and the dissipation due to heat losses [59–62]. This concept can be mathematically formalized as follows:

$$E_{\text{abs}} = E_{\text{th}}^{\text{melt}} + E_{\text{melt}} + E_{\text{th}}^{\text{boil}}, \tag{4}$$

where E_{abs} represents the energy absorbed by the NP, $E_{\text{th}}^{\text{melt}}$ represents the thermal energy necessary to reach the melting point T_m, E_{melt} represents the melting energy, and $E_{\text{th}}^{\text{boil}}$ represents the thermal energy from the melting point to the boiling point T_b. These quantities are, respectively, estimated by the following equations:

$$E_{\text{abs}} = \sigma_{\text{abs}}^{\lambda} \Phi t_p, \tag{5}$$

where $\sigma_{\text{abs}}^{\lambda}$ is the absorption cross section at a given wavelength λ, Φ the laser irradiance (in watts per square meter), and t_p is the pulse duration;

$$E_{\text{th}}^{\text{melt}} = m C_p^{\text{sol}} \Delta_{T_0}^{T_m} T, \tag{6}$$

where m and C_p^{sol} the NP mass and heat capacity of the solid, respectively;

$$E_{\text{melt}} = m L_m, \tag{7}$$

where L_m is the latent heat of fusion;

$$E_{\text{th}}^{\text{boil}} = m C_p^{\text{liq}} \Delta_{T_m}^{T_b} T, \tag{8}$$

where C_p^{liq} is the heat capacity of the liquid NP material. From the previous equations, we can determine Φ_{melt}—the threshold irradiance at which NPs suffer a solid-liquid phase transition for a laser wavelength set at 532 nm. Φ_{melt} can be expressed as follows:

$$\Phi_{\text{melt}} = \frac{E_{\text{th}}^{\text{melt}} + E_{\text{melt}}}{\sigma_{\text{abs}}^{532} t_p}. \tag{9}$$

Several quantities depend on the NP radius r, the composition x, or both. The previous equation is therefore expressed in its expanded form as follows:

$$\Phi_{\text{melt}} = \frac{m(r,x)\left\{C_p^{\text{sol}}(x)\left[T_m(r,x) - T_0\right] + L_m(r,x)\right\}}{\sigma_{\text{abs}}^{532}(r,x) t_p}. \tag{10}$$

The fusion temperature is radius and composition dependent and is calculated with the equation given by Buffat and Borel [63]:

$$T_m(r,x) = T_m^{\text{bulk}}(x)\left\{1 - \frac{2}{r\rho_s(x)L_m(x)} \times \left[\sigma_s(x) - \sigma_l(x)\left(\frac{\rho_s(x)}{\rho_l(x)}\right)^{2/3}\right]\right\}, \tag{11}$$

where $T_m^{\text{bulk}}(x)$ is the melting point of the bulk alloy, taken from the phase diagram, ρ_s and ρ_l are the densities of the solid and liquid alloys, respectively, and σ_s and σ_l are the surface energies of the solid and liquid alloys, respectively.

The cross sections are calculated as follows [64]:

$$\sigma_{\text{abs}}^{\lambda}(r,x) = \sigma_{\text{ext}}^{\lambda}(r,x) - \sigma_{\text{sca}}^{\lambda}(r,x), \tag{12}$$

$$\sigma_{\text{sca}}^{\lambda} = \frac{2\pi}{k^2}\sum_{n=1}^{\infty}(2n+1)\left(|a_n|^2 + |b_n|^2\right), \tag{13}$$

$$\sigma_{\text{ext}}^{\lambda} = \frac{2\pi}{k^2}\sum_{n=1}^{\infty}(2n+1)\ \text{Re}(a_n + b_n), \tag{14}$$

where n is the multipole order and $k = 2\pi n_r/\lambda$, with n_r the real part of the refractive index. The details of the calculation of the coefficients a_n and b_n can be found in the literature [65].

The refractive indices of pure copper and silver were taken from Johnson *et al.* [66]. For the Cu-Ag alloy, data for different compositions (90, 70, 50, and 40 at. % Cu) are available in Ref. [67]. The evolution of $\sigma_{\text{abs}}^{532}$ is presented in Fig. 6(a). The dashed lines represent the contribution of the different multipoles. It is obvious that in the present case (metallic alloys), the contribution of the magnetic multipoles is negligible compared with that of the electric multipoles.

Φ_{melt} is calculated for the full composition range and for radii between 1 and 500 nm (i.e., up to the initial average size of the particles in the micropowders) [Fig. 6(b)]. In Fig. 6(b), one can notice that reaching the melting point of pure silver NPs requires an irradiance that is about 1 order of magnitude higher than for pure Cu NPs of the same size. The experimental irradiance, equal to 3×10^{11} W/m^2 is also plotted in Fig. 6(b). It turns out that the irradiance used is sufficient to melt NPs with radii less than 75 nm, irrespective of their composition. This radius corresponds

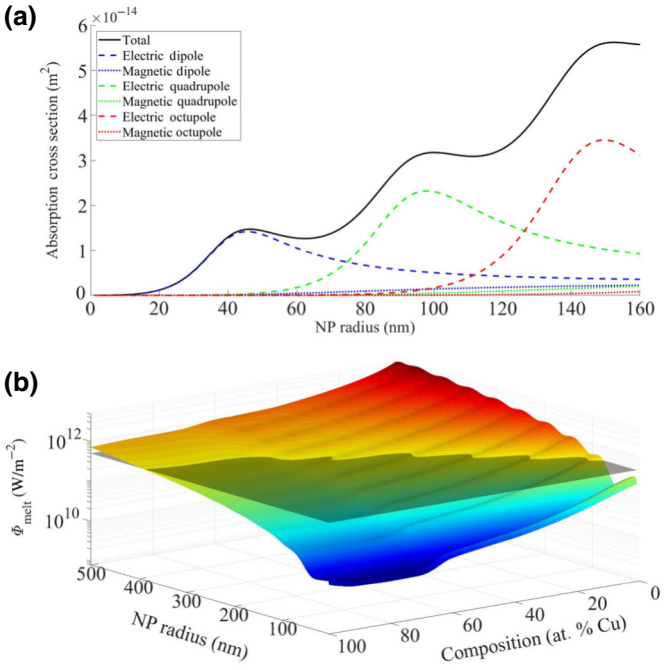

FIG. 6. (a) NP-radius dependence of the absorption cross section of a 50 at. % NP composition, with the contribution of the different multipoles in dashed lines. (b) Melting irradiance as a function of the NP size and composition versus the experimental irradiance, in black, corresponding to $\Phi = 3 \times 10^{11}\,\mathrm{W/m^2}$.

to the largest Ag NP that can be melted under these conditions of irradiance and pulse duration. On the other side of the composition range, the critical radius for pure Cu NPs is about 5 times that of Ag NPs and is 390 nm.

It is worth noting that the model presented does not take into account dissipative energy fluxes. Generally, they can be of two kinds, radiative and convective [59–62,65]. The radiative flux φ_{rad} can be estimated using the Stefan-Boltzmann law:

$$\varphi_{\mathrm{rad}}(r,x) = 4\pi r^2 \sigma_{\mathrm{S\text{-}B}} T_{\mathrm{NP}}^4(r,x), \tag{15}$$

where $\sigma_{\mathrm{S\text{-}B}} = 5.67 \times 10^{-8}\,\mathrm{W/m^2\,K^4}$ is the Stefan-Boltzmann constant and T_{NP} is the NP temperature. The convective flux φ_{conv} is estimated as follows:

$$\varphi_{\mathrm{conv}}(r,c) = 4\pi r^2 h[T_{\mathrm{NP}}(r,c) - T_b], \tag{16}$$

where T_b is the liquid boiling temperature (351 K) and h is the heat-transfer coefficient, which is determined by NP parameters (temperature, diameter, shape) and by the properties of the surrounding medium. The h values can be evaluated on the basis of the Nusselt number Nu,

$$h = \frac{\mathrm{Nu} \times k}{L}, \tag{17}$$

which for spherical particles is expressed using the empirical formula [68]

$$\mathrm{Nu} = 2 + \frac{0.589\mathrm{Ra}^{1/4}}{[1 + (0.469/\mathrm{Pr})^{9/16}]^{4/9}}, \tag{18}$$

where Ra and Pr are, respectively, the Rayleigh number and the Prantl number, which can be expressed as a function of the Grashof number Gr:

$$\mathrm{Ra} = \mathrm{Pr} \times \mathrm{Gr}, \tag{19}$$

$$\mathrm{Pr} = \frac{\mu C}{k}, \tag{20}$$

$$\mathrm{Gr} = \frac{L^3 \rho^2 g \Delta T \beta}{\mu^2}, \tag{21}$$

where k is the thermal conductivity, μ is the viscosity, ρ is the density, C is the specific heat, β is the coefficient of thermal expansion of the surrounding liquid, L is the characteristic length (diameter of the NP in our case), g is the gravitational acceleration, and ΔT is the temperature difference between the heated NPs and the surrounding liquid. For NPs with radius in the range from 1 to 500 nm surrounded by liquid ethanol, h varies from 167 to 0.3 $\mathrm{MW/m^2\,K}$, respectively.

Finally, the dissipative fluxes can be compared with the input flux φ_{input} generated by the laser irradiation, which is expressed as:

$$\varphi_{\mathrm{input}}(r,c) = \sigma_{\mathrm{abs}}^{\lambda}(r,c)\Phi. \tag{22}$$

To do so, upper and lower boundaries of both T_{NP} and σ_{abs} have to be set. For the absorption cross section, it appears that the highest values are obtained for pure copper NPs and the lowest values are obtained for pure silver NPs regardless the NP radius. For the NP temperature, the upper boundary condition T_{max} can be set as the highest boiling point—here that of copper—$T_{\mathrm{max}} = 2835$ K. The lower boundary corresponds to the boiling point of ethanol $T_b^{\mathrm{eth}} = 351$ K. The calculated energy fluxes (input and dissipative) are plotted in Fig. 7, which shows that the input flux overcomes the radiative flux by at least 1 order of magnitude for 1-nm NPs, 2 orders of magnitude for 10-nm NPs, and 3 orders of magnitude for 100-nm NPs. Therefore, it is possible to ignore the radiative losses in heating modeling. The convective flux may overcome the incoming flux for particles smaller than 50 nm. However, this strongly depends on the physical state (liquid or gas) of the surrounding environment.

For small NPs the incoming and convective fluxes are comparable; however, the energy dissipated from the heated nanoparticles into the surrounding liquid might be sufficient to induce local evaporation of the liquid in the vicinity of the NPs [69]. The physics of the nucleation

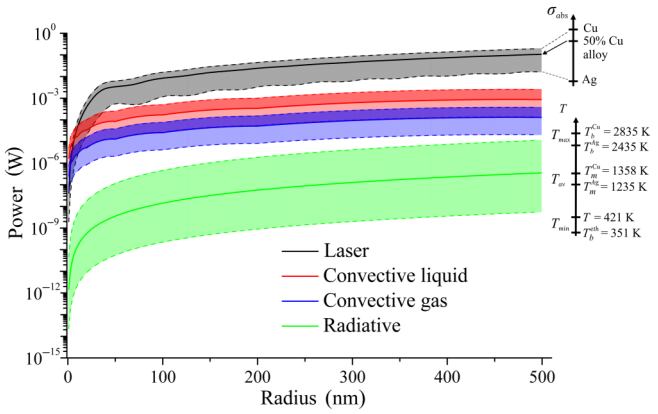

FIG. 7. Comparison of the incoming energy flux from laser irradiation and the radiative and convective dissipations as a function of NP size.

of such gas bubbles under such extreme transient conditions is still debated. The formation of a gaseous envelope around the NPs affects the absorption cross section of the NPs as well as heat dissipation because the heat-transfer coefficient in this case varies from 25 to 0.05 $\mathrm{MW/m^2\,K}$, respectively, for NPs with radius ranging from 1 to 500 nm. The convective flux from the particles surrounded by ethanol vapor is presented in Fig. 7 (blue area).

A good criterion to estimate the probability of forming a bubble consists in comparing the pulse duration t_p with the diffusion time constant τ_d [70]:

$$\tau_d = \frac{r^2}{D_{\mathrm{eth}}}, \tag{23}$$

where D_{eth} is the thermal diffusivity of ethanol taken as $7 \times 10^{-8}\,\mathrm{m^2/s}$. τ_d equals t_p for a NP with a radius of 26 nm and $5t_p$ for a NP with a radius of 59 nm. The formation of a bubble is likely to occur for NPs smaller than 26 nm and unlikely to occur for NPs larger than 59 nm. Therefore, it is more relevant to compare the incoming flux with the convective flux in a vapor in Fig. 7. This shows that for $T = T_{\mathrm{av}}$, the dissipation is more important than the incoming flux for $r < 2.8$ nm, meaning that NPs below this size are not melted. The incoming flux overcomes the convective flux by 1 order of magnitude for a radius larger than 8.1 nm.

Beyond the simple power balance, the formation of a bubble also affects the laser-NP interactions. If the absorption cross section primarily depends on both the initial NP diameter and the initial composition it is also affected by the presence of a gaseous shell. One can see that the cross section is typically reduced by a factor of 3–5 when the shell thickness equals the NP radius. In other words, the experimental irradiance needed to reach the melting point would have to be increased by the same factor. Consequently, in the diffusion region, the melting criterion $\kappa^{\mathrm{CS}}_{\mathrm{melt}}$ can be reformulated as follows:

$$\kappa^{\mathrm{CS}}_{\mathrm{melt}}(r, r_{\mathrm{shell}}, x) = \frac{\Phi(r,x)}{\Phi_{\mathrm{melt}}(r,x)} \times \frac{\sigma^{\mathrm{CS}}_{\mathrm{abs}}(r, r_{\mathrm{shell}}, x)}{\sigma^{0}_{\mathrm{abs}}(r,x)} \tag{24}$$

This criterion is compared with the melting criterion $\kappa_{\mathrm{melt}} = \Phi/\Phi_{\mathrm{melt}}$ without a gas bubble in Fig. 8 (melting occurs if $\kappa_{\mathrm{melt}} > 1$). One can see that in this latter case the melting criterion is fulfilled within the whole composition range within this diffusion region, with a noticeable difference in the κ_{melt} values in the Cu-rich and Ag-rich regions. However, in the case of the presence of a gaseous shell, the melting criterion is fulfilled only up to 95 at. % silver.

The possibility to melt NPs by laser irradiation, and therefore to homogenize the size and composition, is summarized in Fig. 9. Several regions can be identified:

(a) Two light-blue regions corresponding to sizes and compositions at which melting cannot occur. For small NPs ($r \leq 2.8$ nm), heat dissipation is too great

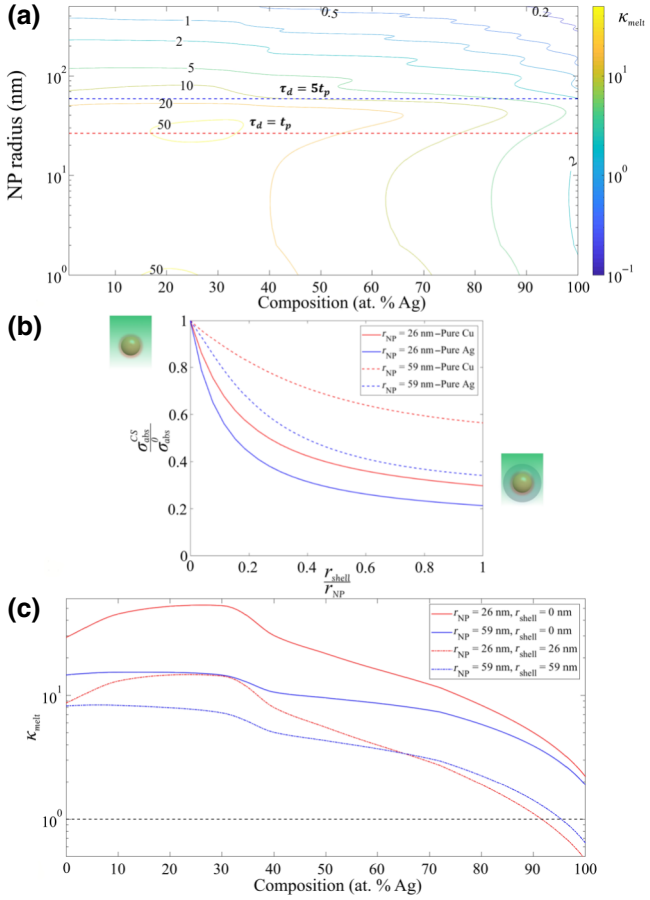

FIG. 8. (a) Dependence of melting criteria on NP radius and composition. (b) Schematic representation of a NP surrounded by a gas bubble and evolution of absorption cross section with gaseous-shell thickness r_{shell}. (c) Comparison of melting criteria for NP with and without a gaseous shell.

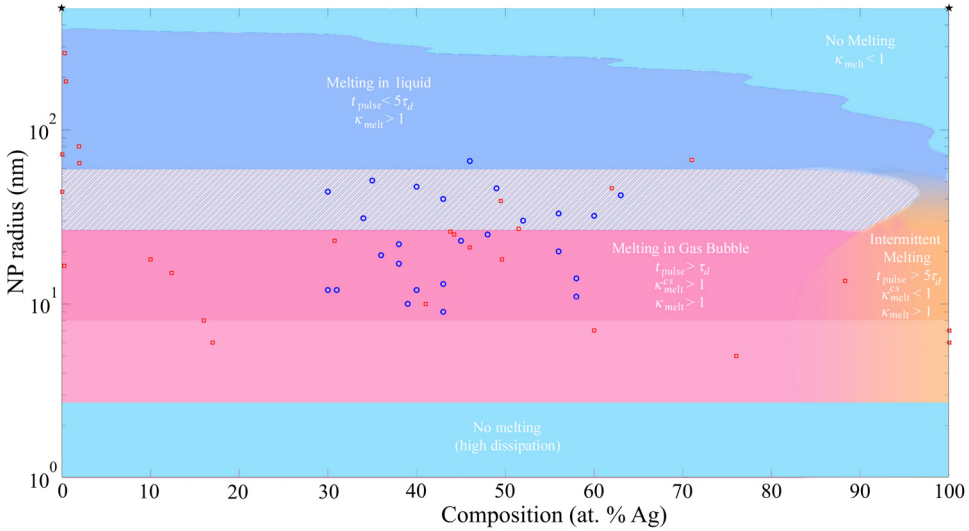

FIG. 9. Size-composition phase diagram overlaid with the melting criterion at irradiance $\Phi = 3 \times 10^{11}$ W/m^2. Initial microparticles, NPs after plasma treatment, and NPs after laser treatment are represented by black stars, red squares, and blue circles, respectively. The hatched area denotes the intermediary zone from melting in the bubble to melting in a liquid, where $\tau_d < t_p < 5\tau_d$, the light-pink area—the boundary zone where incoming and convective fluxes are comparable.

to allow melting. For larger size ($r \geq 390$ nm for pure copper and $r \geq 75$ nm for pure silver), the energy deposited by the laser pulse is insufficient and does not reach the total energy to induce melting.

(b) A light-pink region ($r \leq 8.1$ nm) representing the conditions for which the dissipative flux is less than 1 order of magnitude smaller than the incoming energy flux. Within this region, melting may happen or not

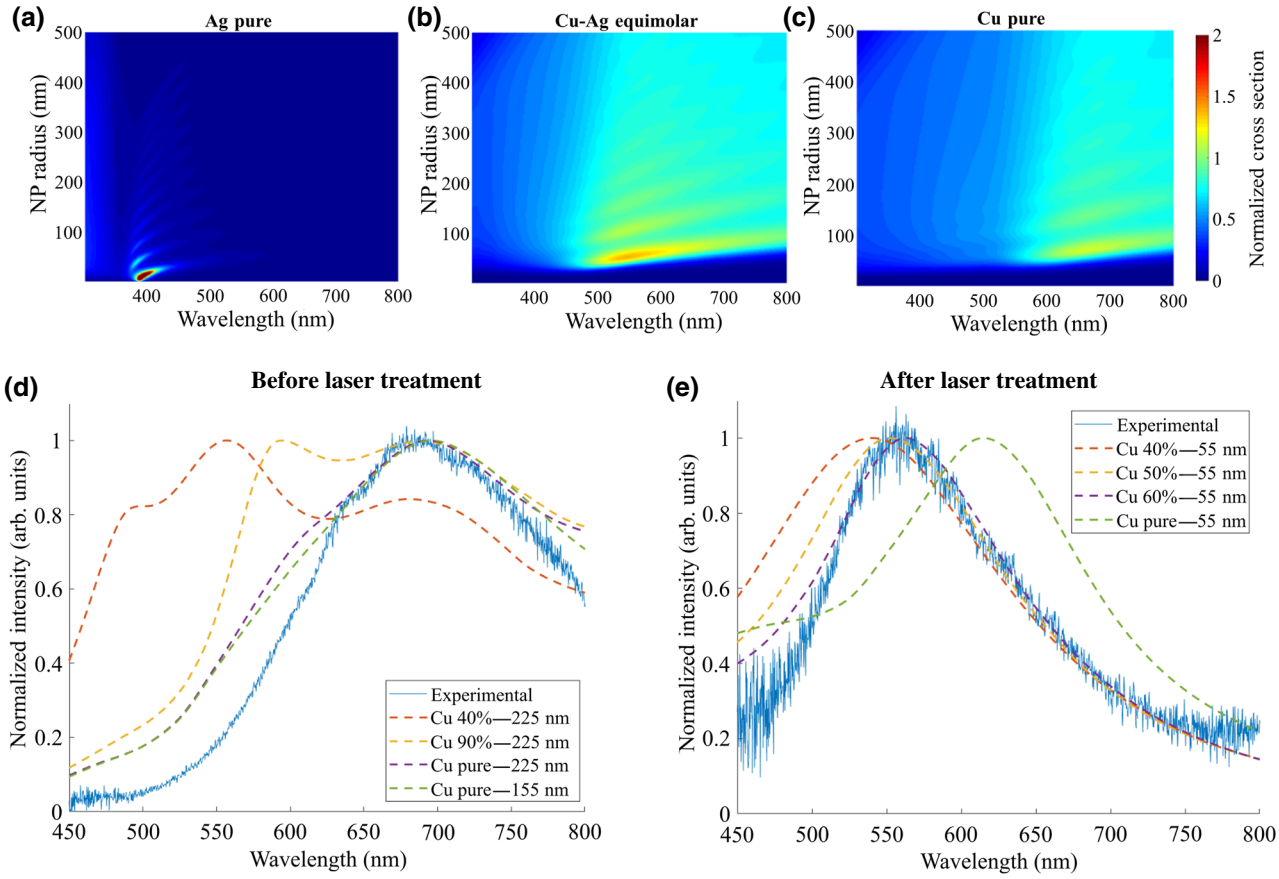

FIG. 10. Analytical calculation of the dependence of the scattering cross section as a function of wavelength and NP radius for different alloy compositions: (a) pure Ag, (b) 50% Cu, and (c) pure Cu. Scattering spectra from Fig. 2(d) (d) before and (e) after laser treatment with modeled spectra for different NP compositions and sizes.

TABLE I. Parameters for identification of spectra.

Parameter	Number of peaks	Peak position (nm)	Peak width (nm)
Before laser treatment	1 or 2	670–730	170–210
After laser treatment	1	560–640	0–150

happen, and the finer determination of the boundary between melting and nonmelting regions requires time-dependent modeling, which will be presented in further work.

(c) A pink region in which the dissipation leads to the formation of a gaseous envelope that decreases the absorption cross section but does not prevent melting.

(d) A dark-blue region in which the dissipation is small compared with the incoming energy flux. Under these conditions, NPs melt in the liquid.

(e) An orange region (on the Ag side) in which a gaseous envelope forms and may affect the possibility to melt NPs. Within this region, the possibility to melt NPs will depend on the time at which the bubble forms as compared with start of the laser pulse. On the one hand, if the bubble forms at the very end of the pulse, the NPs are likely to melt. On the other hand, if the bubble forms at the very beginning of the laser pulse, then the NPs will not melt. The determination of bubble dynamics is particularly complex. However, since no pure Ag NPs are found after laser treatment, it seems that the bubble forms sufficiently late to allow melting.

Figure 9 shows that the initial micropowders with a particle radius of 500 nm could not have been melted and therefore alloyed by the laser irradiation at this irradiance. However, the plasma pretreatment modifies the size and composition distribution towards a region in which laser-induced melting is possible. Although the melting conditions differ in terms of the presence of the bubble or the importance of the dissipation, the laser process results in homogenization of both the size and the composition of NPs, which clearly demonstrates the synergetic effect of combined plasma and laser processing.

B. Optical properties of NPs

The challenge to understand the relationship between the microstructure of NPs and their optical properties relies on the fact that optical dark-field spectroscopy probes about λ^3 (typically 0.05–0.5 μm^3 in the visible range), while TEM reaches atomic scale. In other terms, on the one hand, TEM gives an accurate measurement of the radius and composition of NPs but without information on their optical properties and, on the other hand, dark-field spectroscopy measures scattering of single NPs, which depends on both the NP radius and the NP composition, without being able to measure them directly. This gap can be filled by modeling the scattering spectra within the full range of sizes and composition (radius ranging from 1 to 500 nm

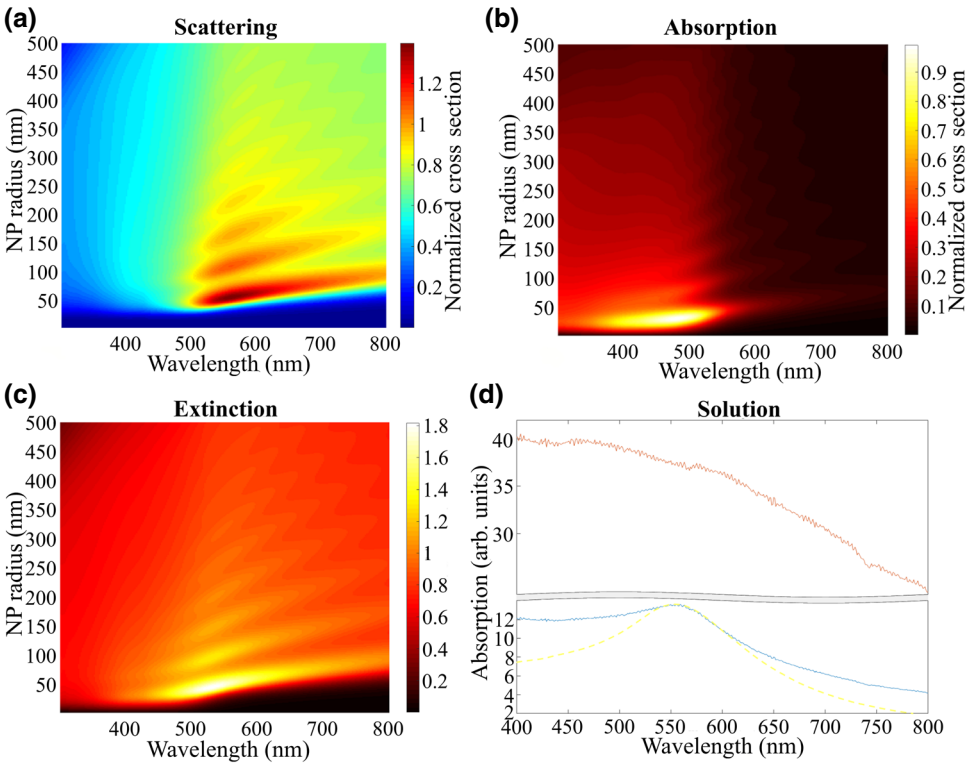

FIG. 11. Analytical calculation of the dependence of the scattering (a), absorption (b), and extinction (c) cross sections for a 60%-Cu-alloy composition. (d) Absorption spectra from colloidal solution before and after laser treatment and the normalized extinction cross section for a 55-nm NP.

and Ag content ranging from 0 to 100 at. %). The calculation is detailed in the previous section. Examples of scattering maps of pure silver, 50% Ag alloy, and pure copper are shown in Figs. 10(a)–10(c), respectively. From these results it appears that the scattering resonances are redshifted with increasing size of the NPs or increasing Cu content. In addition, an increasing NP radius leads to broadening of the scattering spectra.

A homemade filtering procedure is developed under a MATLAB environment to identify, among the 3500 simulated spectra, the scattering spectra matching experimental data. The input parameters are the number of peaks, their position, and their width. The parameters used are summarized in Table I and are determined from the analysis of several tens of scattering spectra from different NPs.

The spectra presented in Fig. 2(b) are corrected by the intensity of the spectrum of the solvent to obtain the sole contribution of NPs [Fig. 11(d)]. The extinction of the colloidal solution is actually composed of both intrinsic absorption of NPs and scattering. Therefore, it is more appropriate to compare the solution absorption with the NP extinction cross-section. The three quantities are represented in Figs. 11(a)–11(c).

Before laser treatment, the absorption spectra do not show any particular features, which is attributed to the large distribution in size and composition. After laser treatment, a particular hump appears around 560 nm [Fig. 11(d)]. A satisfactory model is obtained by our setting the extinction cross section as that of NPs with a radius of 55 nm and a Cu content of 60%. The acceptable mismatch in the profile before 500 nm and after 650 nm may be attributed to the dispersion in size and composition.

V. CONCLUSION

In this paper, we show the synergic effect of combining two nonequilibrium processes based on plasmas and lasers for the synthesis of alloyed NPs. Plasma appears to be efficient to rapidly decrease the mean size of microparticles to sufficiently small NPs and to enable their melting by laser irradiation in a second step. This latter stage contributes to homogenization of the NPs in size and composition. The formation of alloyed Ag-Cu nanocrystals is proved by UV-vis spectroscopy, EDS, and high-resolution TEM measurements. It is shown that alloyed Ag-Cu particles are partially formed after the first step of electrical discharge treatment. However, these particles have a broad size distribution and a nonuniform inner structure. Additional laser treatment results in an increase in size of the small particles along with a decrease in size of large particles and subsequent narrowing of the size distribution. The EDS mapping shows the uniform distribution of the metallic elements in the particles, which is indicative of alloyed-NP formation. The experimental observation of alloying of Ag and Cu NPs is supported by laser-heating modeling of NPs in a liquid based on the balance between the absorbed and dissipated energy fluxes. The modeling reveals the critical radii of Cu NPs (390 nm) and Ag NPs (75 nm) for melting under the selected experimental conditions of irradiance ($\Phi = 3 \times 10^{11}$ W/m^2) and pulse duration (10 ns). Theoretical consideration of dissipative fluxes also allows the proposal of criteria for bubble formation around a particle during its laser heating. Heat dissipation by the convective liquid from the particle is shown to be important. For the heating process, the absorption cross section of one NP under laser irradiation must account for its size and composition dependence. It is shown that in the case of the formation of a gaseous shell around a NP, the melting criterion is fulfilled only up to 95 at. % Ag. Laser-treated NPs demonstrate plasmon-induced scattering of light in the 560–640-nm region. The laser-treatment step is also useful to transform the turbid and colorless solution, resulting from the plasma treatment, into a solution with well-defined absorption in the orange region (560 nm). The combination of both processes opens the way to alternative designs of NPs with controlled properties.

ACKNOWLEDGMENTS

A.N. is grateful to the ITMO Fellowship program for financial support. T.B., S.B., and J.G. benefited from the Programme Hubert Curien-Kolmogorov. T.B. and H.K. are grateful to the Agence Nationale de la Recherche for financial support through the CEENEMA ANR-15-CE05-0005 project. N.T., M.N., and N.T. acknowledge financial support from the Belarusian Foundation for Fundamental Research under Grant No. F 18MS-005. S.M. acknowledges the Ministry of Education and Science of the Russian Federation (project 16.8939.2017/8.9). V.M. thanks the Russian Foundation for Basic Research (project 18-32-20089 molaved).

[1] G. Prieto, J. Zečevič, H. Friedrich, K. P. de Jong, and P. E. de Jongh, Plasma nanoscience: From nano-solids in plasmas to nano-plasmas in solids, Nat. Mater. **12**, 34 (2013).

[2] W. J. E. Beek, M. M. Wienk, and R. a. J. Janssen, Efficient hybrid solar cells from zinc oxide nanoparticles and a conjugated polymer, Adv. Mater. **16**, 1009 (2004).

[3] S. Choudhury, R. Mangal, A. Agrawal, and L. A. Archer, A highly reversible room-temperature lithium metal battery based on crosslinked hairy nanoparticles, Nat. Commun. **6**, 10101 (2015).

[4] Y. Jiao, D. Han, Y. Ding, X. Zhang, G. Guo, J. Hu, D. Yang, and A. Dong, Fabrication of three-dimensionally interconnected nanoparticle superlattices and their lithium-ion storage properties, Nat. Commun. **6**, 6420 (2015).

[5] N. A. Frey, S. Peng, K. Cheng, and S. Sun, Magnetic nanoparticles: Synthesis, functionalization, and applications in bioimaging and magnetic energy storage, Chem. Soc. Rev. **38**, 2532 (2009).
[6] M. V. Zyuzin, D. G. Baranov, A. Escudero, I. Chakraborty, A. Tsypkin, E. V. Ushakova, F. Kraus, W. J. Parak, and S. V. Makarov, Photoluminescence quenching of dye molecules near a resonant silicon nanoparticle, Sci. Rep. **8**, 6107 (2018).
[7] M. V. Yezhelyev, X. Gao, Y. Xing, A. Al-Hajj, S. Nie, and R. M. O'Regan, Emerging use of nanoparticles in diagnosis and treatment of breast cancer, Lancet Oncol. **7**, 657 (2006).
[8] A. S. Timin, A. R. Muslimov, M. V. Zyuzin, O. O. Peltek, T. E. Karpov, I. S. Sergeev, A. I. Dotsenko, A. A. Goncharenko, N. D. Yolshin, A. Sinelnik, B. Krause, T. Baumbach, M. A. Surmeneva, R. V. Chernozem, G. B. Sukhorukov, and R. A. Surmenev, Multifunctional scaffolds with improved antimicrobial properties and osteogenicity based on piezoelectric electrospun fibers decorated with bioactive composite microcapsules, ACS Appl. Mater. Interfaces **10**, 34849 (2018).
[9] J.-H. Park, C. Park, H. Yu, J. Park, S. Han, J. Shin, S. H. Ko, K. T. Nam, Y.-H. Cho, and Y. Park, Subwavelength light focusing using random nanoparticles, Nat. Photonics **7**, 454 (2013).
[10] G. V. Naik, V. M. Shalaev, and A. Boltasseva, Alternative plasmonic materials: Beyond gold and silver, Adv. Mater. **25**, 3264 (2013).
[11] K. Domanski, J.-P. Correa-Baena, N. Mine, M. K. Nazeeruddin, A. Abate, M. Saliba, W. Tress, A. Hagfeldt, and M. Graetzel, Not all that glitters is gold: Metal-migration-Induced degradation in perovskite solar cells, ACS Nano **10**, 6306 (2016).
[12] M. Grzelczak, J. Pérez-Juste, P. Mulvaney, and L. M. Liz-Marzán, Shape control in gold nanoparticle synthesis, Chem. Soc. Rev. **37**, 1783 (2008).
[13] S. Chen, Z. L. Wang, J. Ballato, S. H. Foulger, and D. L. Carroll, Monopod, bipod, tripod, and tetrapod gold nanocrystals, J. Am. Chem. Soc. **125**, 16186 (2003).
[14] Y. Yao, Z. Huang, P. Xie, S. D. Lacey, R. J. Jacob, H. Xie, F. Chen, A. Nie, T. Pu, M. Rehwoldt, D. Yu, M. R. Zachariah, C. Wang, R. Shahbazian-Yassar, J. Li, and L. Hu, Carbothermal shock synthesis of high-entropy-alloy nanoparticles, Science **359**, 1489 (2018).
[15] Z. Peng and H. Yang, Designer platinum nanoparticles: Control of shape, composition in alloy, nanostructure and electrocatalytic property, Nano Today **4**, 143 (2009).
[16] R. He, Y.-C. Wang, X. Wang, Z. Wang, G. Liu, W. Zhou, L. Wen, Q. Li, X. Wang, X. Chen, J. Zeng, and J. G. Hou, Facile synthesis of pentacle gold-copper alloy nanocrystals and their plasmonic and catalytic properties, Nat. Commun. **5**, 4327 (2014).
[17] N. Tien Khi, H. Baik, H. Lee, J. Yoon, J.-H. Sohn, and K. Lee, Rationally synthesized five-fold twinned core-shell Pt_3Ni@Rh nanopentagons, nanostars and nanopaddle-wheels for selective reduction of a phenyl ring of phthalimide, Nanoscale **6**, 11007 (2014).
[18] S. V. Makarov, M. I. Petrov, U. Zywietz, V. Milichko, D. Zuev, N. Lopanitsyna, A. Kuksin, I. Mukhin, G. Zograf, E. Ubyivovk, D. A. Smirnova, S. Starikov, B. N. Chichkov, and Y. S. Kivshar, Efficient second-harmonic generation in nanocrystalline silicon nanoparticles, Nano Lett. **17**, 3047 (2017).
[19] K. Ostrikov, E. C. Neyts, and M. Meyyappan, Plasma nanoscience: From nano-solids in plasmas to nano-plasmas in solids, Adv. Phys. **62**, 113 (2013).
[20] R. J. Mehta, C. Karthik, W. Jiang, B. Singh, Y. Shi, R. W. Siegel, T. Borca-Tasciuc, and G. Ramanath, High electrical conductivity antimony selenide nanocrystals and assemblies, Nano Lett. **10**, 4417 (2010).
[21] I. Levchenko, K. Bazaka, O. Baranov, R. M. Sankaran, A. Nomine, T. Belmonte, and S. Xu, Lightning under water: Diverse reactive environments and evidence of synergistic effects for material treatment and activation, Appl. Phys. Rev. **5**, 021103 (2018).
[22] G. Monastyrsky, Nanoparticles formation mechanisms through the spark erosion of alloys in cryogenic liquids, Nanoscale. Res. Lett. **10**, 503 (2015).
[23] X. Hu, X. Shen, O. Takai, and N. Saito, Facile fabrication of PtAu alloy clusters using solution plasma sputtering and their electrocatalytic activity, J. Alloys Compd. **552**, 351 (2013).
[24] G. Saito and T. Akiyama, Nanomaterial synthesis using plasma generation in liquid, J. Nanomater. **2015**, 123696 (2015).
[25] H. Kabbara, J. Ghanbaja, C. Noël, and T. Belmonte, Synthesis of Cu-ZnO core-shell nanoparticles by spark discharges in liquid nitrogen, Nano-Struct. Nano-Objects **10**, 22 (2017).
[26] Z. Abdullaeva, E. Omurzak, C. Iwamoto, H. Okudera, M. Koinuma, S. Takebe, S. Sulaimankulova, and T. Mashimo, High temperature stable WC_{1-x}@C and TiC@C core-shell nanoparticles by pulsed plasma in liquid, RSC Adv. **3**, 513 (2012).
[27] A. Hamdan, H. Kabbara, C. Noël, J. Ghanbaja, A. Redjaimia, and T. Belmonte, Synthesis of two-dimensional lead sheets by spark discharge in liquid nitrogen, Particuology **40**, 152 (2018).
[28] D. Zhang, B. Gökce, and S. Barcikowski, Laser synthesis and processing of colloids: Fundamentals and applications, Chem. Rev. **117**, 3990 (2017).
[29] G. Gal, Y. Monsa, V. Ezersky, and I. Bar, Alloying copper and palladium nanoparticles by pulsed laser irradiation of colloids suspended in ethanol, RSC Adv. **8**, 33291 (2018).
[30] N. G. Semaltianos, R. Chassagnon, V. Moutarlier, V. Blondeau-Patissier, M. Assoul, and G. Monteil, Nanoparticles alloying in liquids: Laser-ablation-generated Ag or Pd nanoparticles and laser irradiation-induced AgPd nanoparticle alloying, Nanotechnology **28**, 155703 (2017).
[31] S. Besner and M. Meunier, Femtosecond laser synthesis of auAg nanoalloys: Photoinduced oxidation and ions release, J. Phys. Chem. C **114**, 10403 (2010).
[32] A. T. Izgaliev, A. V. Simakin, G. A. Shafeev, and F. Bozon-Verduraz, Intermediate phase upon alloying Au-Ag nanoparticles under laser exposure of the mixture of individual colloids, Chem. Phys. Lett. **390**, 467 (2004).
[33] I. Vassalini, L. Borgese, M. Mariz, S. Polizzi, G. Aquilanti, P. Ghigna, A. Sartorel, V. Amendola, and I. Alessandri,

Enhanced electrocatalytic oxygen evolution in au-fe nanoalloys, Angew. Chem. Int. Ed. **56**, 6589 (2017).

[34] V. Amendola, M. Meneghetti, O. M. Bakr, P. Riello, S. Polizzi, D. H. Anjum, S. Fiameni, P. Arosio, T. Orlando, C. d. J. Fernandez, F. Pineider, C. Sangregorio, and A. Lascialfari, Coexistence of plasmonic and magnetic properties in Au_89Fe_11 nanoalloys, Nanoscale **5**, 5611 (2013).

[35] S. Ibrahimkutty, P. Wagener, T. d. S. Rolo, D. Karpov, A. Menzel, T. Baumbach, S. Barcikowski, and A. Plech, A hierarchical view on material formation during pulsed-laser synthesis of nanoparticles in liquid, Sci. Rep. **5**, 16313 (2015).

[36] A. V. Kabashin, P. Delaporte, A. Pereira, D. Grojo, R. Torres, T. Sarnet, and M. Sentis, Nanofabrication with pulsed lasers, Nanoscale Res. Lett. **5**, 454 (2010).

[37] S. Link, C. Burda, M. B. Mohamed, B. Nikoobakht, and M. A. El-Sayed, laser photothermal melting and fragmentation of gold nanorods: Energy and Laser pulse-width dependence, J. Phys. Chem. A **103**, 1165 (1999).

[38] J. H. Hodak, A. Henglein, M. Giersig, and G. V. Hartland, Laser-induced inter-diffusion in AuAg Core–Shell nanoparticles, J. Phys. Chem. B **104**, 11708 (2000).

[39] H. Wang, A. Pyatenko, K. Kawaguchi, X. Li, Z. Swiatkowska-Warkocka, and N. Koshizaki, Selective pulsed heating for the synthesis of semiconductor and metal submicrometer spheres, Angew. Chem. Int. Ed. **49**, 6361 (2010).

[40] Z. Swiatkowska-Warkocka, A. Pyatenko, F. Krok, B. R. Jany, and M. Marszalek, Synthesis of new metastable nanoalloys of immiscible metals with a pulse laser technique, Sci. Rep. **5**, 9849 (2015).

[41] J. Zhang, J. Worley, S. Denommee, C. Kingston, Z. Jakubek, Y. Deslandes, M. Post, B. Simard, N. Braidy, and G. Botton, Synthesis of metal alloy nanoparticles in solution by laser irradiation of a metal powder suspension, J. Phys. Chem. B **107**, 6920 (2003).

[42] P. R. Subramanian and J. H. Perepezko, The ag-cu (silver-copper) system, J. Phase Equilib. **14**, 62 (1993).

[43] Y. Lei, F. Chen, Y. Jin, and Z. Liu, Ag-Cu nanoalloyed film as a high-performance cathode electrocatalytic material for zinc-air battery, Nanoscale Res. Lett. **10**, 197 (2015).

[44] P. P. Kiran, B. N. Shivakiran Bhaktha, D. N. Rao, and G. De, Nonlinear optical properties and surface-plasmon enhanced optical limiting in ag-cu nanoclusters co-doped in SiO_2 sol-gel films, J. Appl. Phys. **96**, 6717 (2004).

[45] L.-u. Rahman, A. Shah, S. K. Lunsford, C. Han, M. N. Nadagouda, E. Sahle-Demessie, R. Qureshi, M. S. Khan, H.-B. Kraatz, and D. D. Dionysiou, Monitoring of 2-butanone using a Ag-Cu bimetallic alloy nanoscale electrochemical sensor, RSC Adv. **5**, 44427 (2015).

[46] S. Das, R. N. P. Vemuri, and T. L. Alford, Enhanced electrical performance of Ag-Cu thin films after low temperature microwave processing, J. Vacuum Sci. Technol. B **31**, 011204 (2012).

[47] O. Oudbashi and A. Shekofteh, Chemical and microstructural analysis of some Achaemenian silver alloy artefacts from Hamedan, western Iran, Periodico di Mineralogia **84**, 419 (2015).

[48] D. Ashkenazi, H. Gitler, A. Stern, and O. Tal, Metallurgical investigation on fourth century BCE silver jewellery of two hoards from Samaria, Sci. Rep. **7**, 40659 (2017).

[49] P. A. Dmitriev, S. V. Makarov, V. A. Milichko, I. S. Mukhin, A. S. Gudovskikh, A. A. Sitnikova, A. K. Samusev, A. E. Krasnok, and P. A. Belov, Laser fabrication of crystalline silicon nanoresonators from an amorphous film for low-loss all-dielectric nanophotonics, Nanoscale **8**, 5043 (2016).

[50] H. Kabbara, J. Ghanbaja, C. Noël, and T. Belmonte, Nano-objects synthesized from Cu, Ag and $Cu_{28}Ag_{72}$ electrodes by submerged discharges in liquid nitrogen, Mater. Chem. Phys. **217**, 371 (2018).

[51] J. Park, R. S. Zhu, and M. C. Lin, Thermal decomposition of ethanol. I. Ab initio molecular orbital/rice-ramsperger-Kassel-Marcus prediction of rate constant and product branching ratios, J. Chem. Phys. **117**, 3224 (2002).

[52] Z. F. Xu, J. Park, and M. C. Lin, Thermal decomposition of ethanol. III. A computational study of the kinetics and mechanism for the $CH_3 + C_2H_5OH$ reaction, J. Chem. Phys. **120**, 6593 (2004).

[53] J. Li, A. Kazakov, and F. L. Dryer, Experimental and numerical studies of ethanol decomposition reactions, J. Phys. Chem. **108**, 7671 (2004).

[54] G. Grim, *Broadening of Spectral Lines in a Plasma* (Mir, Moscow, 1978).

[55] T. Belmonte, C. Noël, T. Gries, J. Martin, and G. Henrion, Theoretical background of optical emission spectroscopy for analysis of atmospheric pressure plasmas, Plasma Sources Sci. Technol. **24**, 064003 (2015).

[56] P. J. Bruggeman, N. Sadeghi, D. C. Schram, and V. Linss, Gas temperature determination from rotational lines in non-equilibrium plasmas: A review, Plasma Sources Sci. Technol. **23**, 023001 (2014).

[57] Y. Zhang, J. R. G. Evans, and S. Yang, Corrected values for boiling points and enthalpies of vaporization of elements in handbooks, J. Chem. Eng. Data **56**, 328 (2011).

[58] A. Hamdan, C. Noel, F. Kosior, G. Henrion, and T. Belmonte, Dynamics of bubbles created by plasma in heptane for micro-gap conditions, J. Acoust. Soc. Am. **134**, 991 (2013).

[59] A. Pyatenko, H. Wang, N. Koshizaki, and T. Tsuji, Mechanism of pulse laser interaction with colloidal nanoparticles, Laser Photonics Rev. **7**, 596 (2013).

[60] N. Tarasenka, V. Kiris, E. Stankevičius, N. Tarasenko, V. Pankov, F. Krčma, P. Gečys, and G. Račiukaitis, Laser irradiation of Gd–Si and Gd–Si–Ge colloid mixtures for the fabrication of compound nanoparticles, ChemPhysChem **19**, 3247 (2018).

[61] N. A. Kirichenko, I. A. Sukhov, G. A. Shafeev, and M. E. Shcherbina, Evolution of the distribution function of Au nanoparticles in a liquid under the action of laser radiation, Quantum Elec. (Woodbury) **42**, 175 (2012).

[62] V. K. Pustovalov, Theoretical study of heating of spherical nanoparticle in media by short laser pulses, Chem. Phys. **308**, 103 (2005).

[63] P. Buffat and J.-P. Borel, Size effect on the melting temperature of gold particles, Phys. Rev. A **13**, 2287 (1976).

[64] G. P. Zograf, M. I. Petrov, D. A. Zuev, P. A. Dmitriev, V. A. Milichko, S. V. Makarov, and P. A. Belov, Resonant non-plasmonic nanoparticles for efficient temperature-feedback optical heating, Nano Lett. **17**, 2945 (2017).

[65] K. Metwally, S. Mensah, and G. Baffou, Fluence threshold for photothermal bubble generation using plasmonic nanoparticles, J. Phys. Chem. C **119**, 28586 (2015).

[66] P. B. Johnson and R. W. Christy, Optical constants of the noble metals, Phys. Rev. B **6**, 4370 (1972).

[67] J. Song, H. Li, J. Li, S. Wang, and S. Zhou, Fabrication and optical properties of metastable cu-ag alloys, Appl. Opt. **41**, 5413 (2002).

[68] K. Jafarpur and M. M. Yovanovich, International journal of heat and mass transfer, Int. J. Heat Mass Transf. **35**, 2195 (1992).

[69] G. Baffou and R. Quidant, Thermo-plasmonics: Using metallic nanostructures as nano-sources of heat, Laser Photonics Rev. **7**, 171 (2013).

[70] G. Baffou, *Thermoplasmonics: Heating Metal Nanoparticles Using Light* (Cambridge University Press, Cambridge, 2017).